Chinese Chemical Letters 34 (2023) 107458

Contents lists available at ScienceDirect

Chinese Chemical Letters

journal homepage: www.elsevier.com/locate/cclet

Cu cluster embedded porous nanofibers for high-performance CO_2 electroreduction

Zhifeng Xin[a,*], Zibo Yuan[a], Jingjing Liu[a], Xinjian Wang[a], Kejing Shen[a], Yifa Chen[b,*], Ya-Qian Lan[b]

[a] *Institute of Molecular Engineering and Applied Chemistry, Anhui University of Technology, Ma'anshan 243002, China*
[b] *Jiangsu Key Laboratory of New Power Batteries, School of Chemistry and Materials Science, Nanjing Normal University, Nanjing 210023, China*

ARTICLE INFO

Article history:
Received 19 January 2022
Revised 12 February 2022
Accepted 22 April 2022
Available online 27 April 2022

Keywords:
Electrocatalysis
Cu cluster
Porous nanofiber
Electrospinning
CO_2RR

ABSTRACT

Metal-doped carbon materials, as one of the most important electrocatalytic catalysts for CO_2 reduction reaction (CO_2RR), have attracted increasing attention. Herein, a series of Cu cluster embedded highly porous nanofibers have been prepared through the carbonization of electro-spun MOF/PAN nanofibers. The obtained Cu cluster doped porous nanofibers possessed fibrous morphology, high porosity, conductivity, and uniformly dispersed Cu clusters, which could be applied as promising CO_2RR catalysts. Specifically, best of them, MCP-500 exhibited high catalytic performance for CO_2RR, in which the Faradaic efficiency of CO (FE_{CO}) was as high as 98% at -0.8 V and maintained above 95% after 10 h continuous electrocatalysis. The high performance might be attributed to the synergistic effect of tremendously layered graphene skeleton and uniformly dispersed Cu clusters that could largely promote the electron conductivity, mass transfer and catalytic activity during the electrocatalytic CO_2RR process. This attempt will provide a new idea to design highly active CO_2RR electrocatalyst.

Carbon neutralization is a major issue concerned by many countries today. The greenhouse gas directly or indirectly generated by natural and human activities can be captured or stored by forest carbon sink and other artificial technology or engineering means [1]. For chemists, what we can do is to convert the emitted CO_2 into fuels or other useful chemicals in an environmentally friendly way and try to keep the concentration carbon dioxide in the atmosphere constant [2]. Various techniques have been used to efficiently store or convert CO_2 [3–5]. Among which, electrocatalytic CO_2 reduction reaction (CO_2RR) as a kind of high efficiency and controllable approach has been regarded as one of the most powerful approaches to transform CO_2 into high-valued energy products (*e.g.*, CO, CH_4, HCOOH and C_2H_5OH) [6–10].

In recent years, diverse materials have been investigated as catalysts in electrocatalytic CO_2RR [11–13], such as metals [14,15], transition metal oxides [16], transition metal chalcogenides [17], metal-free 2D materials [18–20] and metal-organic frameworks (MOFs) [21–23]. Among all the metal containing catalysts, Cu is the most promising candidate that can convert CO_2 into various kinds of products, like CO, CH_4, C_2H_4, and C_2H_5OH, *etc.* [24,25]. Many related factors can affect the catalytic activity and selectivity of Cu-based catalysts [10,26,27]. Among many influencing factors, controlling the particle size of Cu can effectively regulate the catalytic activity and selectivity of electrocatalytic CO_2RR [28]. Therefore, the investigation of Cu nanoparticles especially that in atomic scale will be an interesting candidate to explore the intriguing properties of electrocatalytic CO_2RR [29].

MOFs with rich and well-dispersed metal centers linked by organic ligands makes them to be excellent precursors to synthesize carbon-based materials with uniformly dispersed active metal sites [30–34]. During the carbonization process, the metal in MOFs is transformed into atomic sized nanoparticle and organic component convert to carbon skeleton [35–37]. The derived composite materials possess unique active sites at the surface/interface, making the catalytic activity more effective. However, it is still easy for metal elements in MOFs to be agglomerated into larger particles due to the scarce carbon source from simply organic ligand, thus it would be difficult to obtain carbon materials doped metal sites in small grains or even monoatomic dispersion. Therefore, a second carbon source or stable complex molecules are usually added into MOF materials before calcination to prevent the metal agglomeration [38]. Recently, many carbon materials containing metal sites have been prepared by using MOFs as the precursors [39–42], such as carbon supported N-coordination Cu-Fe diatomic catalyst [43], Ni single atom catalyst [38], nickel-cobalt bimetal phos-

---

* Corresponding authors.
E-mail addresses: xinzf521@ahut.edu.cn (Z. Xin), chyf927821@163.com (Y. Chen).

https://doi.org/10.1016/j.cclet.2022.04.056

phide nanotubes [44] or hollow particle-based nitrogen-doped carbon nanofibers [45]. However, the strategies reported were still restricted by the bottlenecks like: (1) the derived bulk form of MOFs after carbonation generally limited the mass transfer and gas diffusion and (2) the lack in conductivity or efficiency for the generation of highly selective electrocatalytic CO_2RR products. Therefore, it is desirable to develop new MOF carbonization strategy that enable the fabrication of MOFs into unique porous morphology with atomic-level dispersed metal active sites that are much beneficial for the mass transfer and conductivity to achieve high-performance electrocatalytic CO_2RR systems [46,47].

In this work, we have developed an electrospinning and carbonization method to prepare Cu cluster doped porous nanofibers. MOF-545-Cu nanoparticles were firstly mixed with polyacrylonitrile (PAN) to form MOF-545-Cu/PAN (MCP) composite nanofibers by electrospinning method. After a subsequent carbonization reaction, primary MOF-545-Cu nanoparticles in PAN matrix were transformed into Cu cluster doped porous nanofibers that were beneficial for increasing the electrocatalytic performance in electrocatalytic CO_2RR. Specifically, MCP-500 exhibited high catalytic performance for CO_2RR, in which the Faradaic efficiency of CO (FE_{CO}) was as high as 98% at −0.8 V and maintained above 95% after 10 h electrocatalysis. The high performance might be attributed to the synergistic effect of tremendously layered graphene skeleton and uniformly dispersed Cu clusters that could largely promote the conductivity and mass transfer to largely improve the catalytic activity of electrocatalytic CO_2RR.

To investigate the catalytic performance, a series of catalysts were prepared as the followed procedures. The synthesis of MOF-545 and MOF-545-Cu was slightly modified according to the reported method [48,49]. The detailed procedure was displayed in the Supporting Information.

Preparation of MOF-545-Cu/PAN nanofibers (MCP fiber): 0.15 g polyacrylonitrile (PNA, average MW 150,000) was dissolved in 5 mL DMF. 0.1 g MOF-545-Cu powder was ground thoroughly and dispersed into the above solution *via* sonication for 1 h, followed by stirring for 24 h to form homogeneously dispersed mixture. Then the mixture was sucked into a 5 mL syringe equipped with a 0.2 mm stainless-steel nozzle, which was connected to a high-voltage power supply. The high voltage is 18 kV between the anode and cathode with 15 cm. The feeding rate is about 1 cm/h. The brick-red MOF-545-Cu/PAN composite fiber (MCP fiber) based membrane was obtained on the aluminum foil and dried at 70 °C overnight under vacuum.

Preparation of CuO/N/C composite fibers: The MCP fiber was carbonized in a tube furnace under the Ar atmosphere. In detail, 0.1 g MCP fiber was placed in a ceramic boat and then the boat was placed in the tube furnace. Sealed the tube furnace and set the gas flow rate at 30 mL/min. After 30 min argon flow, it was firstly heated at 220 °C for 1 h and further heated to 500 °C with a heating rate of 2 °C/min. After heating at 500 °C for 2 h, MCP-500 was obtained. MCP-400, MCP-600 and MCP-800 were prepared using similar process, except that they were annealed at 400 °C, 600 °C and 800 °C for 2 h, respectively. The samples of MC-500, PAN-500 and MP-500 were obtained by calcining MOF-545-Cu, PAN and MOF-545/PAN fiber at 500 °C using the same heating processes, respectively.

The synthetic procedure for Cu cluster dopped nanofibers was depicted in Fig. 1. In a typical procedure, MOF-545-Cu nanoparticle was firstly embedded into PAN (MCP) nanofibers by an electrospinning method. After a heating at a certain temperature under Ar atmosphere, the PAN molecule and organic ligands in MOF-545-Cu decomposed and converted into N-doped carbon materials. Meanwhile, the Cu^{2+} species chelated with 4 N of TCPP in MOF-545-Cu nanoparticles was reduced to uniformly dispersed metallic Cu clusters, during which the chelation of TCPP and the doping of PAN molecules prevented the aggregation of Cu to some extent. With the increase of calcination temperature, the Cu specie in the fiber aggregated into larger particles. The optimized Cu cluster doped nanofiber was obtained through carbonizing the MCP fiber at 500 °C for 2 h.

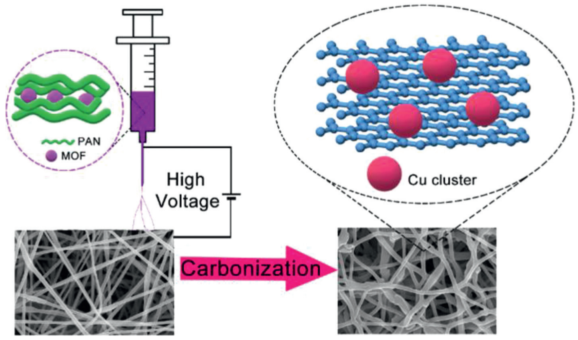

Fig. 1. Schematic illustration of the synthesis of Cu cluster-doped porous nanofibers (MCP-500).

To determine the composition and structure of the MCP nanofiber, powder X-ray diffraction (PXRD), field-emission scanning electron microscopy (FESEM), N_2 sorption and EDS measurement were carried out. The PXRD pattern of MCP fiber showed the characteristic diffraction peaks of MOF-545-Cu, indicating MOF-545-Cu nanoparticle was successfully embedded into PAN nanofiber (Fig. S1c in Supporting information). The broad peaks between 20° and 30° can be ascribed to the amorphous phase of PAN. As revealed by the FESEM test (Fig. S1e in Supporting information), the as-prepared MOF-545-Cu/PAN showed fibrous morphology with an average diameter of about 200 nm. The EDS element mapping showed that C, N and Cu were uniformly dispersed in the nanofiber, which clearly displayed that MOF-545-Cu was embedded in the PAN nanofiber (Fig. S1f in Supporting information). Besides, the N_2 sorption tests have been conducted and showed that the specific S_{BET} of MCP fiber (21.2 m^2/g) was higher than pure PAN fiber (12.6 m^2/g), which indicated that the loading of MOF nanoparticles increased the surface area of the nanofiber (Fig. S1d in Supporting information). Besides, TGA measurements of MOF-545-Cu/PAN and pure PAN nanofibers were carried out under N_2 atmosphere. The TGA curves of PAN fiber and MOF-545-Cu/PAN (Fig. S2 in Supporting information) displayed that the low weight loss before 350 °C attributed to the so-called cyclization reaction, which was accompanied by the release of hydrogen cyanide or ammonia [50]. The weight loss from 350 °C to 550 °C belonged to the carbonization and decomposition of PAN and MOF-545-Cu, and the weight loss above 550 °C would be ascribed to the further decomposition and carbonization of PAN and MOF-545-Cu. The above results set basis for the further calcination and electrocatalysis investigation.

After heating at 400, 500 and 600 °C under Ar atmosphere, the organic ligands in MOF-545-Cu and PAN molecules were decomposed and converted into N-doped carbon materials. And Cu in MOF-545-Cu migrated and aggregated into Cu nanoparticles embedded in N-C skeleton. The phase of the samples calcined at 400, 500 and 600 °C were characterized by PXRD tests (Fig. 2a). The broad peaks among the range from 20° to 30° indicate the amorphous phase of carbon materials. The sharp peak at 26° corresponded to the crystal plane (002) of graphene (PDF card No. 26-1076). The weak peak of MCP-500 and MCP-600 at 43.3° corresponded to the crystal plane (111) of Cu (PDF card No. 89-2838), which indicated the small crystal grain was formed at 500 and 600 °C [51]. Raman spectra show that the graphitization degree of carbon materials increases with the increase of calcination temperature (Fig. 2b). Interestingly, the characteristic peak of Cu was

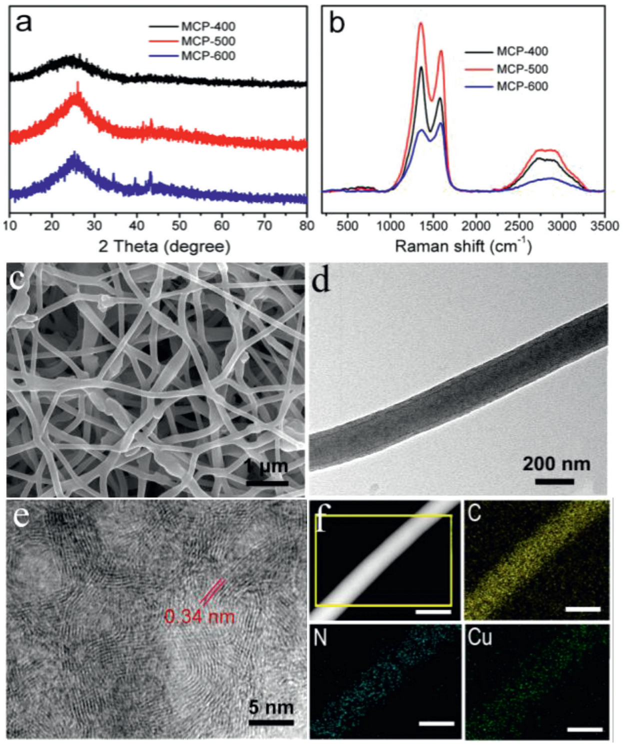

Fig. 2. Characterization of the obtained samples. (a) PXRD patterns and (b) Raman spectra of the samples of MCP-400, MCP-500 and MCP-600. (c) SEM image (d) TEM image. (e) HRTEM image (f) STEM image and elemental mapping of MCP-500. (the scale bar is 200 nm).

not found in the PXRD pattern of MCP-400, which might attribute to that Cu atom did not aggregate to large particles at 400 °C. The characteristic peaks of Cu become more obvious with the increase of temperature, which indicated that the Cu atom in Cu-TCPP tends to migrate and assembled to larger particles, with the increase of the temperature. This result can also be evidenced by the later HRTEM images. To further investigate the effect of PAN on the structure and morphology of MOF in the calcination process, pure MOF-545-Cu nanoparticle was calcined at 500 °C. TEM image showed the shrunk rodlike morphology (Fig. S3c in Supporting information) compared with MOF-545-Cu particles (Fig. S3b in Supporting information) after treating at 500 °C. HRTEM images (Fig. S3d in Supporting information) displayed no continuous carbon structure and obvious Cu particles in the sample, which can also be illustrated by the clear characteristic peaks of CuO and Cu in PXRD pattern (Fig. S3e in Supporting information). And the EDS elements mapping (Fig. S3f in Supporting information) indicated the uniformly dispersed of C, N, Cu, O and Zr in the particles. The results indicated that the addition of the second carbon source was beneficial for the formation of continuous carbon skeleton and prevention of metal aggregation.

To deeply investigate the morphology of the calcined nanofibers, TEM measurement was carried out. The SEM and TEM image showed that MCP-500 still maintained the nanofiber morphology (Figs. 2c and d) with a diameter of ~200 nm. The HRTEM image showed continuous layered structure (Fig. 2e), and the lattice distance (0.34 nm) is in accordance with the interlayer distance of graphite. The elemental mapping displayed that the C, N and Cu elements was uniformly dispersed in the nanofiber (Fig. 2f). The HRTEM image of MCP-500 displayed the small Cu particle with the diameter of 0.4 nm uniformly dispersed in the carbon skeleton (Fig. S4 in Supporting information). After calcining at 400 °C, the nanofiber still maintained smooth surface and the average diameter (~200 nm) remained almost the same as that of MCP-400 (Figs. S5a and b in Supporting information). However, the HRTEM image showed the amorphous structure, which would properly attribute to the treating at relatively lower temperature. When the calcination temperature raised to 600 °C, the nanofiber still maintained smooth surface and the diameter slightly shrunk to ~180 nm (Figs. S6a and b in Supporting information). The HRTEM image showed the noncontinuous crystalline graphene particles, and Cu nanoparticles appeared with the size about 5 nm for MCP-600 (Fig. S6c in Supporting information), which was also consistent with the results of PXRD test. The EDS elemental mapping results indicate that the elements of C, N, O, Zr and Cu were evenly dispersed in MCP-600 (Fig. S6d in Supporting information). With the increase of temperature, the Cu content (Table S1 and Fig. S7 in Supporting information) gradually increased from 1.4% (MCP-400) to 1.8% (MCP-500) and further to 2.4% (MCP-600), indicating the varied decomposition effects of organic component under different treating temperatures. To investigate the pore structure of calcined materials, the N_2 sorption measurements were carried out. The N_2 sorption measurements (Fig. S8 in Supporting information) indicated that the composite carbon nanofibers displayed high porosity, and the S_{BET} of MCP-400, MCP-500 and MCP-600 is about 26 m^2/g, 77 m^2/g and 95 m^2/g, respectively, and the pore distribution were very wide. The porosity structure was benefit to the diffusion of carbon dioxide and products.

To investigate the state of Cu element in the calcined materials, the samples were analyzed by X-ray photoelectron spectroscopy (XPS) and the results were shown in Fig. S9 (Supporting information). The high-resolution Cu 2p spectra in MCP-500 fitted into two peaks at 932.0 and 952.0 eV were attributed to Cu $2p_{3/2}$ and Cu $2p_{1/2}$ for Cu^+, respectively. In addition, peaks at 934.2 and 954.0 eV were ascribed to Cu $2p_{3/2}$ and Cu $2p_{1/2}$ for Cu^{2+}, implying the mixed valance of Cu^+ and Cu^{2+} in MCP-500. In the high-resolution Cu 2p spectra of MCP-400, two peaks at 931.78 and 951.55 eV are attributed to Cu $2p_{3/2}$ and Cu $2p_{1/2}$ for Cu^{2+}, respectively [50–54]. However, the XPS high-resolution Cu 2p spectra in MCP-600 and MCP-500 showed two peaks at 932.8 eV and 952.56 eV for Cu $2p_{3/2}$ and Cu $2p_{1/2}$ of Cu^0, respectively. These results presented the valance change of samples under different calcination temperature.

To study the electrocatalytic CO_2RR performance, the linear sweep voltammetry (LSV) curves showed the current changing trend with the increasing of voltage. MCP-500 presented a low onset potential of −0.3 V and a large total current density of 35 mA/cm^2 at −1.1 V which was larger than that of MCP-400 and MCP-600 (Fig. 3a). The higher current density of MCP-500 reflected the higher electrocatalysis activity for CO_2RR compared with MCP-400 and MCP-600. To further investigate the electrochemical properties of MCP-500, the LSV curves were tested in Ar-saturated $KHCO_3$ solution, and it showed a much smaller current density than that in CO_2-saturated $KHCO_3$ solution, indicating the high electrochemical performance of MCP-500 came from CO_2RR (Fig. 3b). To further study the decomposition condition of the composite nanofiber, MCP-800 was prepared by calcinated at 800 °C. The SEM image (Fig. S10a in Supporting information) showed the fiber was broken and particles were obvious seen on the surface. TEM image (Fig. S10b in Supporting information) displayed the particles aggregated fiber and poor carbon in the fiber, and HRTEM further demonstrated that the fiber was decomposed into particles at 800 °C. The PXRD (Fig. S10e in Supporting information) exhibited Cu and Cu_2O phase in the fiber. While the catalytic performance (Fig. S10f in Supporting information) was much lower for the large particles and lack of carbon media.

In addition, the FEs of MCP-500 and various contrast samples have been tested. The gas chromatogram shows that CO was the main gas product for MCP-500, and the ^1H NMR spectrum indicated no liquid product was detected (Fig. S11 in Supporting in-

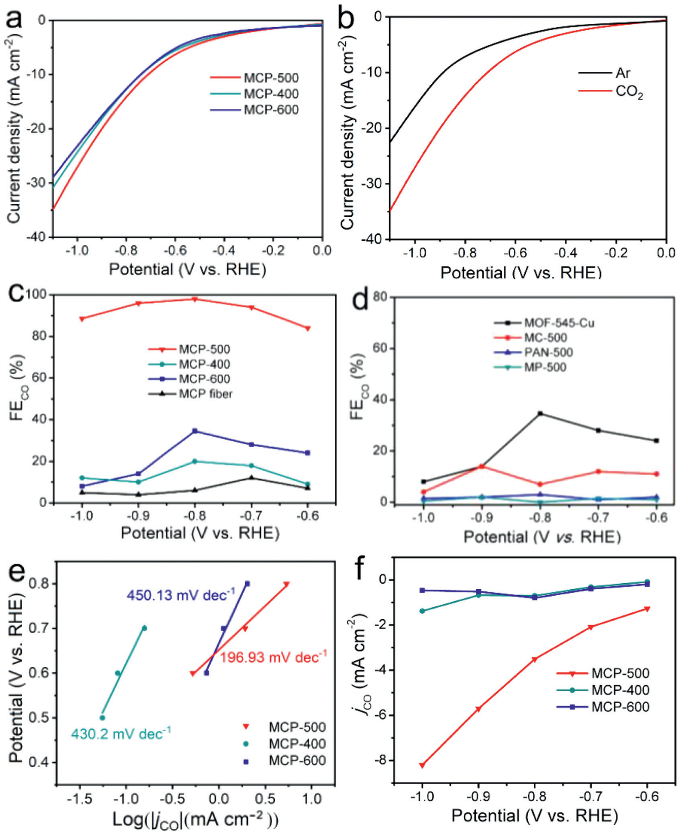

Fig. 3. Electrocatalytic properties of the calcined samples: (a) LSV of MCP-400, MCP-500, MCP-600. (b) LSV of MCP-500 measured at CO_2 and Ar-saturated $KHCO_3$ solution. (c) FE_{CO} of MCP fiber and MCP-400, MCP-500, MCP-600. (d) FE_{CO} of MOF-545-Cu, MC-500, PAN-500. (e) Tafel plots and (f) Partial CO current density for MCP-400. MCP-500, MCP-600 and MP-500. MC-500, PAN-500 and MP-500 are the sample of MOF-545-Cu, PAN nanofiber and MOF-545/PAN nanofiber calcined at 500 °C, respectively.

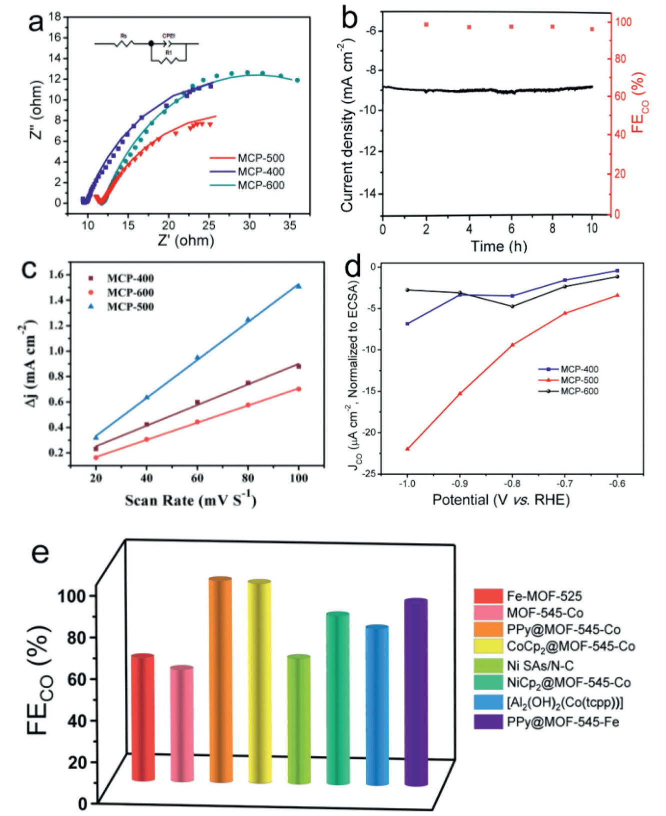

Fig. 4. Electrocatalytic performance of the calcined samples: (a) Nyquist plots of MCP-500, MCP-400 and MCP-600. (b) Durability test of MCP-500 at the potential of −0.7 V *vs.* RHE. (c) The calculated C_{dl} for MCP-500, MCP-400 and MCP-600. (d) ECSA-normalized CO partial current density of MCP-500, MCP-400 and MCP-600, and the calculated C_{dl} for MCP-500, MCP-400 and MCP-600 is 14.9, 8.1 and 6.7 mF/cm^2, respectively. (e) A summary of electrocatalytic performances of the literature reported MOFs and derived materials from MOF.

formation). Moreover, the FEs and current density are carried out to evaluate the electrocatalytic CO_2RR properties of contrast samples (*i.e.*, MCP-400, MCP-600, MC-500, MOF-545-Cu, MOF-545). As shown in Fig. 3c, the maximum FE_{CO} for MCP-500 reached to 98% at −0.8 V and maintains high FE_{CO} (>80%) from −0.6 V to −1.0 V. In contrast, the MOF-545-Cu (35%, −0.8 V) and MCP fiber (11.4%, −0.7 V) exhibited much lower FE_{CO} owing to the poor electron transfer ability (Figs. 3c and d). Furthermore, the corresponding maximum FE_{CO} value for MCP-500 (98%) was also much higher than that of MP-500 (2.5%), MC-500 (14%) and PAN-500 (5%).

The lower CO_2 reduction catalytic performance of MP-500 and PAN-500 than MCP-500 might be attributed to the absence of metal catalytic sites. Moreover, the lower catalytic activity of MC-500 would be ascribed to its lower electron transfer efficiency owing to the lack of sufficient electron transfer medium in the sample. What is more, PAN-500 and MP-500 showed almost no catalytic activity for CO_2RR (Fig. 3d). Therefore, the high FE of MCP-500 could be attributed to the high electron transfer ability and activity caused by the continuous layered graphene structure and high active metal sites.

Tafel slope was an important parameter to quantify the amount of additional applied potential required to observe the logarithmic increase in the measured current, which was often applied to characterize the performance of an electrochemical catalyst [53]. The smaller the slope of Tafel curve, the lower the overpotential of the catalytic process under the same kinetic current density. In the electrocatalytic CO_2RR process, the reaction kinetics for the CO formation is elucidated by the Tafel slopes (Fig. 3e). The Tafel slope of MCP-500 (196.93) was largely smaller than MCP-400 (430.2) and MCP-600 (450.13), indicating more favorable kinetic of MCP-500 to generate CO at the same condition than MCP-400 and MCP-600. To further investigate the intrinsic activity of MCP-400, MCP-500 and MCP-600, the electrochemical active surface area (ECSA) was evaluated by the double-layer capacitance (C_{dl}) according to cyclic voltammetry (CV) measurements at different scan rates (Fig. S12 in Supporting information) [54]. As revealed by the Nyquist plots (Fig. 4a), the charge-transfer resistance (R_{ct}) of MCP-500 (31.98 Ω) was lower than that of MCP-400 (33.88 Ω) and MCP-600 (39.34 Ω), implying the higher charge-transfer rate for MCP-500. Besides, the partial CO current density was evaluated to reveal the activity of the samples. MCP-500 exhibited a high value of −8.2 mA/cm^2 at −1.0 V, which was much higher than MCP-400 (−1.4 mA/cm^2 at −1.0 V) and MCP-600 (−0.8 mA/cm^2 at −0.8 V) (Fig. 4b). The C_{dl} of MCP-400, MCP-500 and MCP-600 were calculated to be 8.11, 14.94 and 6.75 mF/cm^2, respectively (Fig. 4c). The higher Tafel slope demonstrated more favorable kinetics of MCP-500 than MCP-400 and MCP-600 for the generation of CO. And the calculated ECSA for MCP-400, MCP-600 and MCP-500 was 202, 168 and 373 cm^2, respectively. The measured ECSA corrected CO partial current density of MCP-500 is obviously higher than MCP-400 and MCP-600 (Fig. 4d), which can be concluded that MCP-500 exhibited higher catalytic activity. Moreover, MCP-500 also exhibited outstanding durability for CO_2RR and the FE_{CO} could maintain at ~95% with almost unchanged current density (9 mA/cm^2) after 10 h of continuous electrolysis at −0.8 V (Fig. 4d). Noteworthy, the catalytic performance (98%, −0.8 V) achieved by MCP-500 was also superior to most of the reported MOFs and MOF-derived materials (Fig. 4e) [33,41,44,49–51].

In summary, we have developed a facile method to prepare a series of Cu cluster doped porous nanofibers and successfully applied them in efficient electrocatalytic CO_2RR. The obtained Cu cluster doped porous nanofibers possessed advantages such as fibrous morphology, high porosity, conductivity, and uniformly dispersed Cu clusters, which were much beneficial for electrocatalytic CO_2RR. Specifically, MCP-500 exhibited excellent catalytic performance for CO_2RR, in which the FE_{CO} was as high as 98% at -0.8 V and it maintained above 95% after 10 h electrocatalysis. The high performance may be attributed to the synergistic effect of continuous layered graphene skeleton and uniformly dispersed copper clusters in the nanofibers. This work provides a new insight for the design of novel CO_2 electroreduction catalysts and would extend the application scope of MOFs in this field.

Declaration of competing interest

The authors declare that they have no known competing financial interests or personal relationships that could have appeared to influence the work reported in this paper.

Acknowledgments

This work was financially supported by the National Natural Science Foundation of China (Nos. 21471003, 21871141, 21871142, 21701085 and 21901122); Natural Science Foundation of Educational Commission of Anhui Province of China (No. KJ2020A0240); the Natural Science Research of Jiangsu Higher Education Institutions of China (No. 19KJB150011) and Project funded by China Postdoctoral Science Foundation (No. 2019M651873).

Supplementary materials

Supplementary material associated with this article can be found, in the online version, at doi:10.1016/j.cclet.2022.04.056.

References

[1] J.D. Shakun, P.U. Clark, F. He, et al., Nature 484 (2012) 49–54.
[2] J. Qiao, Y. Liu, F. Hong, J. Zhang, Chem. Soc. Rev. 43 (2014) 631–675.
[3] N.M. Dowell, P.S. Fennell, N. Shah, G.C. Maitland, Nat. Clim. Change 7 (2017) 243–249.
[4] T.C. Zhuo, Y. Song, G.L. Zhuang, et al., J. Am. Chem. Soc. 143 (2021) 6114–6122.
[5] S. Fu, S. Yao, S. Guo, et al., J. Am. Chem. Soc. 143 (2021) 20792–20801.
[6] P.Q. Liao, J.Q. Shen, J.P. Zhang, Coord. Chem. Rev. 373 (2018) 22–48.
[7] Y. Pan, R. Lin, Chen Y, et al., J. Am. Chem. Soc. 140 (2018) 4218–4221.
[8] J. Jiao, R. Lin, S. Liu, et al., Nat. Chem. 11 (2019) 222–228.
[9] H. Rao, L.C. Schmidt, J. Bonin, M. Robert, Nature 548 (2017) 74–77.
[10] P.D. Luna, R. Quintero-Bermudez, C.T. Dinh, et al., Nat. Catal. 1 (2018) 103–110.
[11] T. Haas, R. Krause, R.M. Weber, M. Demler, G. Schmid, Nat. Catal. 1 (2018) 32–39.
[12] D.D. Zhu, J.L. Liu, S.Z. Qiao, Adv. Mater. 28 (2016) 3423–3452.
[13] S. Zhao, Y. Wang, J. Dong, et al., Nat. Energy 1 (2016) 16184–16193.
[14] Q. Li, J. Fu, W. Zhu, et al., J. Am. Chem. Soc. 139 (2017) 4290–4293.
[15] W. Zhang, Y. Hu, L. Ma, et al., Adv. Sci. 5 (2018) 1700275.
[16] S. Gao, Y. Lin, X. Jiao, et al., Nature 529 (2016) 68–71.
[17] M. Asadi, C. Liu, A. Addepalli, et al., Science 353 (2016) 467–470.
[18] X. Duan, J. Xu, Z. Wei, et al., Adv. Mater. 29 (2017) 1701784.
[19] Z.Y. Sun, T. Ma, H.C. Tao, Q. Fan, B. Han, Chem 3 (2017) 560–587.
[20] S. Zhao, D.W. Wang, R. Amal, et al., Adv. Mater. 31 (2019) 1801526.
[21] L. Ye, J. Liu, Y. Gao, L. Dai, J. Mater. Chem. A 4 (2016) 15320–15326.
[22] Y. Wang, P. Hou, Z. Wang, P. Kang, ChemPhysChem 18 (2017) 3142–3147.
[23] L.M. Rodriguez-Albelo, A.R. Ruiz-Salvador, A. Sampieri, et al., J. Am. Chem. Soc. 131 (2009) 16078–16087.
[24] D. Raciti, C. Wang, ACS Energy Lett. 3 (2018) 1545–1556.
[25] S. Nitopi, E. Bertheussen, S.B. Scott, et al., Chem. Rev. 119 (2019) 7610–7672.
[26] K. Klingan, T. Kottakkat, Z.P. Jovanov, et al., ChemSusChem 11 (2018) 3449–3459.
[27] J. Huang, M. Mensi, E. Oveisi, V. Mantella, R. Buonsanti, J. Am. Chem. Soc. 141 (2019) 2490–2499.
[28] C.W. Li, M.W. Kanan, J. Am. Chem. Soc. 134 (2012) 7231–7234.
[29] J. Gao, H. Wang, K. Feng, et al., Mater. Adv. 1 (2020) 2286–2292.
[30] Y. Zheng, S.Z. Qiao, Natl. Sci. Rev. 5 (2018) 626–627.
[31] L. Jiao, H.L. Jiang, Chem 5 (2019) 786–804.
[32] C. He, J. Liang, Y.H. Zou, et al., Nat. Sci. Rev. 9 (2022) nwab157.
[33] J. Liang, Q. Wu, Y.B. Huang, R. Cao, EnergyChem 3 (2021) 100064.
[34] Y. Hou, Y.B. Huang, Y.L. Liang, et al., CCS Chem. 1 (2019) 384–395.
[35] E. Luo, H. Zhang, X. Wang, et al., Angew. Chem. Int. Ed. 58 (2019) 12469–12475.
[36] H. Zhang, S. Wang, M. Wang, et al., J. Am. Chem. Soc. 139 (2017) 14143–14149.
[37] M. Zhang, Q. Dai, H. Zheng, M. Chen, L. Dai, Adv. Mater. 30 (2018) 1705431.
[38] Y.N. Gong, L. Jiao, Y. Qian, et al., Angew. Chem. Int. Ed. 59 (2020) 2705–2709.
[39] S.S. Sankar, K. Karthick, K. Sangeetha, et al., J. Mater. Chem. A 9 (2021) 11961–12002.
[40] L. Song, T. Xu, D. Gao, et al., Chem. Eur. J. 25 (2019) 6621–6627.
[41] Z. Li, J. Bu, C. Zhang, et al., New J. Chem. 45 (2021) 10672–10682.
[42] W. Gu, J. Lv, B. Quan, et al., J. Alloy. Compd. 806 (2019) 983–991.
[43] R. Yun, F. Zhan, X. Wang, et al., Small (2020) 2006951.
[44] L. Pan, T. Muhammad, L. Ma, et al., Appl. Catal. B: Environ. 189 (2016) 181–191.
[45] C. Yu, Y. Wang, J. Cui, et al., J. Mater. Chem. A 6 (2018) 8396–8404.
[46] L.F. Chen, Y. Lu, L. Yu, X.W. Lou, Energy Environ. Sci. 10 (2017) 1777–1783.
[47] L. Lin, H. Li, C. Yan, et al., Adv. Mater. 31 (2019) 1903470.
[48] P. Grégoire, G.M. Maria, R.M. Catherine, et al., J. Am. Chem. Soc. 140 (2018) 3613–3618.
[49] Z. Xin, Y.R. Wang, Y. Chen, et al., Nano Energy 67 (2020) 104233.
[50] A.R. Horrocks, J. Zhang, M.E. Hall, Polym. Int. 33 (1994) 303–314.
[51] W.H. Cheng, Appl. Catal. A: General 130 (1995) 13–15.
[52] W.L. Dai, Q. Sun, J.F. Deng, W. Dong, Y.H. Sun, Appl. Surf. Sci. 177 (2001) 172.
[53] A.M. Limaye, J.S. Zeng, A.P. Willard, K. Manthiram, Nat. Commun. 12 (2021) 703.
[54] H. Cheng, X. Wu, M. Feng, et al., ACS Catal. 11 (2021) 12673–12681.